Study of ion turbulent transport and profile formations using global gyrokinetic full-*f* Vlasov simulation

2009 Nucl. Fusion 49 065029

(http://iopscience.iop.org/0029-5515/49/6/065029)

IOP Publishing and International Atomic Energy Agency — Nuclear Fusion

Nucl. Fusion **49** (2009) 065029 (14pp) doi:10.1088/0029-5515/49/6/065029

Study of ion turbulent transport and profile formations using global gyrokinetic full-f Vlasov simulation

Y. Idomura[1], **H. Urano**[2], **N. Aiba**[2] and **S. Tokuda**[2]

[1] Japan Atomic Energy Agency, Higashi-Ueno 6-9-3, Taitou, Tokyo 110-0015, Japan
[2] Japan Atomic Energy Agency, Mukouyama 801-1, Naka, Ibaraki 311-0193, Japan

Received 29 December 2008, accepted for publication 16 April 2009
Published 26 May 2009
Online at stacks.iop.org/NF/49/065029

Abstract

A global gyrokinetic toroidal full-f five-dimensional Vlasov simulation GT5D (Idomura *et al* 2008 *Comput. Phys. Commun.* **179** 391)is extended including sources and collisions. Long time tokamak micro-turbulence simulations in open system tokamak plasmas are enabled for the first time based on a full-f gyrokinetic approach with self-consistent evolutions of turbulent transport and equilibrium profiles. The neoclassical physics is implemented using the linear Fokker–Planck collision operator, and the equilibrium radial electric field E_r is determined self-consistently by evolving equilibrium profiles. In ion temperature gradient driven turbulence simulations in a normal shear tokamak with on-axis heating, key features of ion turbulent transport are clarified. It is found that stiff ion temperature T_i profiles are sustained with globally constant $L_{ti} \equiv |T_i/T_i'|$ near a critical value, and a significant part of the heat flux is carried by avalanches with $1/f$ type spectra, which suggest a self-organized criticality. The E_r shear strongly affects the directions of avalanche propagation and the momentum flux. Non-diffusive momentum transport due to the E_r shear stress is observed and a non-zero (intrinsic) toroidal rotation is formed without momentum input near the axis.

PACS numbers: 52.30.Gz, 52.35.Ra, 52.65.Tt

(Some figures in this article are in colour only in the electronic version)

1. Introduction

Five-dimensional (5D) gyrokinetic simulations are essential tools to study anomalous turbulent transport in tokamak plasmas [2–6]. Although a number of gyrokinetic simulations have been developed so far, most of the existing simulations are δf simulations in an isolated system without sources and collisions or in an open system with fixed gradients. In a δf approach, only the perturbed distribution function δf is solved by forcing the equilibrium distribution f_0 to be fixed. δf gyrokinetic simulations with fixed gradients have been successful in estimating steady transport levels for profiles observed in experiment (see e.g. [6]). However, it still has difficulty in addressing open issues such as the profile stiffness, transient transport properties and the formation of transport barriers [6]. In particular, it is very difficult to simulate turbulent transport with stiff profiles, because the experimental data contain finite errors and a slight change in fixed gradients leads to a large increase in turbulent transport [7]. To resolve this issue, a recent advanced gyrokinetic δf simulation adopts an approach in which equilibrium profiles are adjusted until turbulent transport levels reach the experimental values, where the balance conditions of particle and heat fluxes are satisfied [4]. By using this approach, ion and electron heat fluxes in the experiment were successfully reproduced [8]. However, when one intends to reproduce the particle transport, the momentum transport and the heat transport for each particle species, simultaneously, one has to optimize all the related equilibrium profiles such as the density, the toroidal rotation, the temperature, the radial electric field and so on at each radial position. This may be a formidable task because turbulent transport often has non-local properties, and several transport channels have off-diagonal terms, which lead to indirect interaction among different transport channels. In addition, global δf simulations normally use an adaptive source model to fix the equilibrium profiles on average [9], and its particle, momentum and heat source profiles also have to match the experiment. On the other hand, in a full-f approach, such flux balance conditions are automatically satisfied by simply imposing experimentally relevant source profiles. Then, one observes turbulent transport and evolving equilibrium profiles, and if these profiles deviate from the experiment, one proceeds to improve physical models. This is the validation process of a full-f approach, which may have less ambiguity.

In addition, former fluid simulations with fixed fluxes or fixed sources [10, 11] revealed an interaction between turbulent transport and equilibrium profiles, where gradients are not fixed but fluctuate near their critical values via avalanche like transport processes with $1/f$ type spectra. This kind of power law in the frequency spectrum is a typical feature of self-organized criticality (SOC) like phenomena [12] and suggest non-local transport properties related to Bohm like features in the tokamak micro-turbulence [13]. Fluid simulations in [11] also showed qualitative and quantitative differences between fixed gradient and fixed flux approaches, which may correspond to δf and full-f approaches in the context of a gyrokinetic simulation. In general, SOC phenomena have a scale free character in space and time. This raises a serious question about the validity of the former approach, in which an evolution equation of δf is derived by assuming a separation of characteristic spatio-temporal scales between f_0 and δf. Another important issue is to simulate the edge turbulence where the perturbation amplitude reaches $\delta f/f_0 \sim \mathcal{O}(1)$. From these backgrounds, recently, developments of global gyrokinetic full-f Vlasov simulations have been started [1, 14–17].

In a full-f approach, turbulent transport and equilibrium profiles are solved self-consistently following the same first principles. In core plasmas, amplitudes of the density fluctuation δn are small compared with the equilibrium density n_0, $\delta n/n_0 < 1\%$, and the normalized collisionality ν^* is very small $\nu^* \ll 1$. In order to treat such small amplitude and weak dissipation phenomena in a full-f approach, we need a numerical scheme which satisfies high accuracy and numerical stability simultaneously. To resolve this requirement, we developed a new non-dissipative conservative finite difference scheme (NDCFD) [18], which keeps the numerical stability by conserving the phase space volume, f, and f^2, which are conservation properties inherent to the gyrokinetic Poisson bracket operator. The NDCFD was successfully applied to a global gyrokinetic toroidal full-f 5D Vlasov code (GT5D) [1], and the code was verified through linear and nonlinear benchmarks of the ion temperature gradient (ITG) driven turbulence against a global gyrokinetic δf 3D particle-in-cell code (GT3D) [19]. In the benchmark, robustness and accuracy of NDCFD were examined, and a possibility of long time full-f gyrokinetic simulations was demonstrated. At the moment, GT5D uses a gyrokinetic model for the ITG turbulence in core plasmas, and will be improved to an extended gyrokinetic model for edge plasmas in future works.

In this work, we extend GT5D including sources and collisions, and develop long time source driven ITG turbulence simulations based on a full-f approach. Source and sink models are needed to simulate open system tokamak plasmas, in which a heat flux is imposed by auxiliary heating. A sink model is closely related to boundary conditions. Since the edge turbulence is out of the scope of this study, the boundary condition of core plasmas is imposed by a sink model reflecting conditions given by edge plasmas. Collisions work as a physical dissipation mechanism of fine scale velocity space structures, which are produced by mixing due to the ballistic mode. From the viewpoint of the entropy balance relation [20–22], such a dissipation mechanism is essential for reaching statistically steady states in long time gyrokinetic turbulence simulations [23]. In addition, the collisional effect or the neoclassical physics itself is an important physics ingredient in gyrokinetic simulations. The neoclassical transport gives a baseline of transport levels, when turbulent transport is quenched, e.g. in transport barriers. The neoclassical physics dictates relevant kinetic equilibrium. In our previous collisionless gyrokinetic simulations, f_0 was chosen as a gyrokinetic Vlasov equilibrium distribution defined by a function of three constants of motion, the canonical toroidal angular momentum P_ζ, the energy ε and the magnetic moment μ [19]. However, particle distributions given by such Vlasov equilibria do not coincide between ions and electrons because of their different orbit widths, and the charge neutrality is not exactly satisfied. This means that we need to determine relevant kinetic equilibria with equilibrium radial electric fields E_r, which are dictated by the neoclassical physics in a perturbative manner. The equilibrium E_r and mean $E_r \times B$ flows play critical roles in turbulent transport. In order to keep the standard neoclassical physics in core plasmas, we implement ion–ion collisions using the linear Fokker–Planck collision operator, and verify it through comparisons against standard local neoclassical theories. In source driven ITG turbulence simulations, we trace long time evolutions of the ITG turbulence and equilibrium profiles in a normal shear tokamak. As a qualitative validation of GT5D, we study stiffness of the ion temperature T_i profile, intermittent transport phenomena and momentum transport in the ITG turbulence, and discuss their correspondence with the experiment.

This paper is organized as follows. In section 2, the gyrokinetic equations, the linear Fokker–Planck collision operator and source models are given, and their numerical methods are explained. In section 3, benchmark calculations of the neoclassical transport phenomena are shown. In section 4, source driven ITG turbulence simulations are presented, and long time behaviour of turbulent transport and profile formations is addressed. Finally, in summary, qualitative comparisons between the present simulation results and the experiment are discussed.

2. Calculation model

In this study, we consider the electrostatic ITG turbulence described by gyrokinetic ions and adiabatic electrons in an axisymmetric toroidal configuration. In the modern gyrokinetic theory [24], the gyrokinetic equation is written using the gyro-centre Hamiltonian,

$$H = \tfrac{1}{2}m_i v_\parallel^2 + \mu B + e\langle\phi\rangle_\alpha, \tag{1}$$

and the gyrokinetic Poisson bracket operator,

$$\begin{aligned}\{F, G\} \equiv \frac{\Omega_i}{B}\left(\frac{\partial F}{\partial \alpha}\frac{\partial G}{\partial \mu} - \frac{\partial F}{\partial \mu}\frac{\partial G}{\partial \alpha}\right) \\ + \frac{\boldsymbol{B}^*}{m_i B_\parallel^*}\cdot\left(\nabla F\frac{\partial G}{\partial v_\parallel} - \frac{\partial F}{\partial v_\parallel}\nabla G\right) \\ - \frac{c}{eB_\parallel^*}\boldsymbol{b}\cdot\nabla F \times \nabla G,\end{aligned} \tag{2}$$

in the gyro-centre coordinates $\boldsymbol{Z} = (t; \boldsymbol{R}, v_\parallel, \mu, \alpha)$, where $\boldsymbol{R}$ is a position of the guiding centre, $v_\parallel$ is the parallel velocity, μ is the magnetic moment, α is the gyro-phase angle, $\boldsymbol{B} = B\boldsymbol{b}$ is the magnetic field, $\boldsymbol{b}$ is the unit vector in the parallel direction, m_i and e are the mass and charge of ions, respectively, c is the velocity of light, $\Omega_i = (eB)/(m_i c)$ is the cyclotron frequency, $B_\parallel^* = \boldsymbol{b}\cdot\boldsymbol{B}^*$ is a parallel component of $\boldsymbol{B}^* = \boldsymbol{B} + (Bv_\parallel/\Omega_i)\nabla\times\mathbf{b}$, ϕ is the electrostatic potential and the gyro-averaging operator is defined as $\langle\cdot\rangle_\alpha \equiv \oint \cdot \mathrm{d}\alpha/2\pi$. By using equations (1) and (2), the gyrokinetic equation in the collisionless and sourceless limit is simply given as the Liouville equation,

$$\begin{aligned}\frac{\mathrm{D}f}{\mathrm{D}t} &\equiv \frac{\partial f}{\partial t} + \{f, H\} \\ &= \frac{\partial f}{\partial t} + \{\boldsymbol{R}, H\}\cdot\frac{\partial f}{\partial \boldsymbol{R}} + \{v_\parallel, H\}\frac{\partial f}{\partial v_\parallel} \\ &= 0,\end{aligned} \tag{3}$$

where f is the guiding centre distribution function, and the nonlinear characteristics are given as

$$\begin{aligned}\dot{\boldsymbol{R}} &\equiv \{\boldsymbol{R}, H\} = \frac{\boldsymbol{B}^*}{m_\mathrm{i}B_\parallel^*}\frac{\partial H}{\partial v_\parallel} + \frac{c}{eB_\parallel^*}\boldsymbol{b}\times\nabla H \\ &= v_\parallel\boldsymbol{b} + \frac{c}{eB_\parallel^*}\boldsymbol{b}\times(e\nabla\langle\phi\rangle_\alpha + m_\mathrm{i}v_\parallel^2\boldsymbol{b}\cdot\nabla\boldsymbol{b} + \mu\nabla B),\end{aligned} \tag{4}$$

$$\begin{aligned}\dot{v}_\parallel &\equiv \{v_\parallel, H\} = -\frac{\boldsymbol{B}^*}{m_\mathrm{i}B_\parallel^*}\cdot\nabla H \\ &= -\frac{\boldsymbol{B}^*}{m_\mathrm{i}B_\parallel^*}\cdot(e\nabla\langle\phi\rangle_\alpha + \mu\nabla B).\end{aligned} \tag{5}$$

Since f and H are gyro-phase independent, the first term in equation (2) vanishes automatically in equations (3)–(5). Equations (4) and (5) satisfy the phase space volume conservation, which is written as an incompressible condition of the Hamiltonian flow,

$$\nabla\cdot(\mathcal{J}\dot{\boldsymbol{R}}) + \frac{\partial}{\partial v_\parallel}(\mathcal{J}\dot{v}_\parallel) = 0, \tag{6}$$

where $\mathcal{J} = m_\mathrm{i}^2 B_\parallel^*$ is the Jacobian of the gyro-centre coordinates. From the phase space volume conservation (6), the gyrokinetic equation (3) yields its conservative form,

$$\frac{\partial \mathcal{J}f}{\partial t} + \nabla\cdot(\mathcal{J}\dot{\boldsymbol{R}}f) + \frac{\partial}{\partial v_\parallel}(\mathcal{J}\dot{v}_\parallel f) = 0. \tag{7}$$

By adding a collision term $C(f)$, a source term S_src and a sink term S_snk, a conservative gyrokinetic equation used in GT5D is written as

$$\begin{aligned}&\frac{\partial \mathcal{J}f}{\partial t} + \nabla\cdot(\mathcal{J}\dot{\boldsymbol{R}}f) + \frac{\partial}{\partial v_\parallel}(\mathcal{J}\dot{v}_\parallel f) \\ &\quad = \mathcal{J}C(f) + \mathcal{J}S_\mathrm{src} + \mathcal{J}S_\mathrm{snk}.\end{aligned} \tag{8}$$

The self-consistency is imposed by the quasi-neutrality condition or the gyrokinetic Poisson equation,

$$\begin{aligned}&-\nabla_\perp\cdot\frac{\rho_\mathrm{ti}^2}{\lambda_\mathrm{Di}^2}\nabla_\perp\phi + \frac{1}{\lambda_\mathrm{De}^2}(\phi - \langle\phi\rangle_\mathrm{f}) \\ &\quad = 4\pi e\left[\int f\delta([\boldsymbol{R}+\rho]-\boldsymbol{x})\,\mathrm{d}^6Z - n_{0\mathrm{e}}\right],\end{aligned} \tag{9}$$

where $\boldsymbol{R}+\rho$ is a particle position, $\mathrm{d}^6Z = m_\mathrm{i}^2 B_\parallel^*\,\mathrm{d}\boldsymbol{R}\,\mathrm{d}v_\parallel\,\mathrm{d}\mu\,\mathrm{d}\alpha$ is the phase space volume of the gyro-centre coordinates, ρ_ti is the Larmor radius evaluated with the thermal velocity v_ti, λ_Di and λ_De are the ion and electron Debye lengths and $\langle\cdot\rangle_\mathrm{f}$ is an integral flux surface average operator involving the geometry coupling effect [2]. In equation (9), the first term in the l.h.s. is an ion polarization effect coming from the first order term of the pull back transformation in the gyrokinetic ordering [24]. In this study, we use a linearized ion polarization term with a long wavelength approximation. This approximation may be valid for the core ITG turbulence, which is characterized by $k_\perp^2\rho_\mathrm{ti}^2 \ll 1$ and $\delta n/n_0 \ll 1$.

In order to implement the neoclassical physics in core plasmas, ion–ion collisions are modelled by the linear Fokker–Planck collision operator [25, 26], which is valid for $\delta f/f_0 \ll 1$:

$$\begin{aligned}C(f) &= \frac{\partial}{\partial s}(\nu_{\perp 1}v^2 f) + \frac{\partial}{\partial u}(\nu_{\parallel 1}uf) + \frac{1}{2}\frac{\partial^2}{\partial s^2}(\nu_{\perp 2}v^4 f) \\ &\quad + \frac{1}{2}\frac{\partial^2}{\partial u^2}(\nu_{\parallel 2}v^2 f) + \frac{\partial^2}{\partial s\partial u}(\nu_{\parallel\perp}v^3 f) + C_\mathrm{F},\end{aligned} \tag{10}$$

where $s = 2\mu B/m_\mathrm{i}$ and $u = v_\parallel - U_\parallel$ are a moving frame with respect to the parallel flow velocity $U_\parallel$ and $v^2 = u^2 + s$. The definitions of the collision frequencies, $\nu_{\perp 1}$, $\nu_{\parallel 1}$, $\nu_{\perp 2}$, $\nu_{\parallel 2}$, $\nu_{\parallel\perp}$, and the field particle operator C_F are given in the appendix. The moving frame and collision frequencies are calculated at each position using evolving equilibrium profiles, which provide indirect nonlinear effects on $C(f)$. Operator (10) is annihilated by a shifted Maxwellian distribution with an arbitrary flow velocity. It is noted that equation (10) is given in the drift-kinetic limit, and we ignore corrections related to finite Larmor radius (FLR) effects to satisfy local conservation properties of the particle number, the momentum and the kinetic energy:

$$\int C(f)m_\mathrm{i}^2 B_\parallel^*\,\mathrm{d}v_\parallel\,\mathrm{d}\mu\,\mathrm{d}\alpha = 0, \tag{11}$$

$$\int m_\mathrm{i}v_\parallel C(f)m_\mathrm{i}^2 B_\parallel^*\,\mathrm{d}v_\parallel\,\mathrm{d}\mu\,\mathrm{d}\alpha = 0, \tag{12}$$

$$\int \left(\tfrac{1}{2}m_\mathrm{i}v_\parallel^2 + \mu B\right)C(f)m_\mathrm{i}^2 B_\parallel^*\,\mathrm{d}v_\parallel\,\mathrm{d}\mu\,\mathrm{d}\alpha = 0, \tag{13}$$

which are basic requirements used in the neoclassical theory [27, 28]. It should be noted that the gyrokinetic Vlasov–Poisson system, equations (8) and (9), naturally reduces to a physical model of the neoclassical theory in the axisymmetric limit with macroscopic radial electric fields E_r. Firstly, it is trivial that for macroscopic perturbations with $k_\perp L \sim \mathcal{O}(1)$, the gyrokinetic equation (8) reduces to the drift-kinetic equation [27]. Here, L is a characteristic scale length of equilibrium profiles. Secondly, by taking the time derivative and the flux-surface average of equation (9) and substituting equation (8), we derive a particle balance relation:

$$\begin{aligned}\frac{\partial}{\partial r}\left[-\left\langle\frac{\rho_\mathrm{ti}^2}{4\pi e\lambda_\mathrm{Di}^2}\right\rangle_\mathrm{f}\frac{\partial E_\mathrm{r}}{\partial t} - \Gamma\right] &= \left\langle\int C(f)m_\mathrm{i}^2 B_\parallel^*\,\mathrm{d}v_\parallel\,\mathrm{d}\mu\,\mathrm{d}\alpha\right\rangle_\mathrm{f} \\ &= 0,\end{aligned} \tag{14}$$

where the particle flux is defined as

$$\begin{aligned}\Gamma &\equiv \left\langle\int f(\dot{\boldsymbol{R}}_0\cdot\nabla r)\delta([\boldsymbol{R}+\rho]-\boldsymbol{x})\,\mathrm{d}^6Z\right\rangle_\mathrm{f} \\ &\simeq \left\langle\int f(\dot{\boldsymbol{R}}_0\cdot\nabla r)m_\mathrm{i}^2 B_\parallel^*\,\mathrm{d}v_\parallel\,\mathrm{d}\mu\,\mathrm{d}\alpha\right\rangle_\mathrm{f} \\ &= \left\langle\int \delta f(\boldsymbol{v}_B\cdot\nabla r)m_\mathrm{i}^2 B_\parallel^*\,\mathrm{d}v_\parallel\,\mathrm{d}\mu\,\mathrm{d}\alpha\right\rangle_\mathrm{f}.\end{aligned} \tag{15}$$

Here, $\dot{\boldsymbol{R}}_0 = \{\boldsymbol{R}, \langle H\rangle_\zeta\}$ is a particle orbit given by an axisymmetric part of the Hamiltonian $\langle H\rangle_\zeta$, $\boldsymbol{v}_B$ is the magnetic drift terms in equation (4), and $\delta f = f - f_{\rm M}$ is a deviation of f from a local Maxwellian distribution $f_{\rm M}$ at each flux surface. When the collision operator conserves the particle number, equation (14) leads to the equation for $E_{\rm r}$:

$$-\left\langle \frac{\rho_{\rm ti}^2}{4\pi e\lambda_{\rm Di}^2}\right\rangle_{\rm f} \frac{\partial E_{\rm r}}{\partial t} = \Gamma, \qquad (16)$$

which was used to determine neoclassical electric fields [29, 30]. Therefore, the present physical model is expected to recover the neoclassical theory in the axisymmetric limit. Equation (16) shows a balance between second order terms in the gyrokinetic ordering, while they are derived from the first order gyro-centre transform. In [31], it was pointed out that the gyrokinetic equations derived from the first order transform in a so-called recursive approach cannot determine macroscopic electric fields. However, the above discussion shows that in the modern gyrokinetic theory, its flux-surface averaged form has high enough accuracy to determine $E_{\rm r}$ even with the first order transform.

A source term requires an empirical modelling. In this study, we simulate heat and momentum transport due to the ITG turbulence driven by on-axis heating with a given power input. On the other hand, at the boundary of core plasmas, we fix the ion temperature $T_{\rm i}$ and the parallel flow $U_\parallel$ on average reflecting boundary conditions in H-mode plasmas, where the pedestal temperature is limited by edge localized modes and a no-slip boundary $U_\parallel = 0$ is imposed by the charge exchange with the neutrals. Following the above consideration, we use models for a heat source $S_{\rm src}$ near the axis and a heat sink $S_{\rm snk}$ in a boundary region:

$$S_{\rm src} = A_{\rm src}(\boldsymbol{R})\tau_{\rm src}^{-1}(f_{\rm M1} - f_{\rm M2}), \qquad (17)$$

$$S_{\rm snk} = A_{\rm snk}(\boldsymbol{R})\tau_{\rm snk}^{-1}(f_0 - f), \qquad (18)$$

where $A_{\rm src}$ and $A_{\rm snk}$ are deposition profiles, $f_{\rm M1}$ and $f_{\rm M2}$ are (shifted) Maxwellian distributions, $\tau_{\rm src}$ and $\tau_{\rm snk}$ are time constants for the energy sink and f_0 is the initial distribution. In equation (17), $A_{\rm src}$, $\tau_{\rm src}$, $f_{\rm M1}$ and $f_{\rm M2}$ are chosen to fix power input without particle and momentum input:

$$\int S_{\rm src} m_{\rm i}^2 B_\parallel^* \,{\rm d}v_\parallel\,{\rm d}\mu\,{\rm d}\alpha = 0, \qquad (19)$$

$$\int m_{\rm i} v_\parallel S_{\rm src} m_{\rm i}^2 B_\parallel^* \,{\rm d}v_\parallel\,{\rm d}\mu\,{\rm d}\alpha = 0, \qquad (20)$$

$$\int \left(\tfrac{1}{2} m_{\rm i} v_\parallel^2 + \mu B\right) S_{\rm src}\,{\rm d}^6 Z = P_{\rm in}, \qquad (21)$$

where $P_{\rm in}$ is power input. In equation (18), $T_{\rm i}$ and $U_\parallel$ in the boundary region are modified towards their initial values by a Krook operator with the time constant $\tau_{\rm snk}$. This model works not only as a heat sink but also as a momentum source (sink) when a negative (positive) momentum flux is absorbed. This kind of momentum source at the boundary is considered as the origin of the intrinsic toroidal rotation.

A power balance in the above gyrokinetic equations is given as follows:

$$\int H\frac{\partial f}{\partial t}\,{\rm d}^6 Z = \frac{{\rm d}E_{\rm kin}}{{\rm d}t} + \frac{{\rm d}E_{\rm fld}}{{\rm d}t} = \frac{{\rm d}E_{\rm col}}{{\rm d}t} + \frac{{\rm d}E_{\rm src}}{{\rm d}t} + \frac{{\rm d}E_{\rm snk}}{{\rm d}t}, \qquad (22)$$

$$\frac{{\rm d}E_{\rm kin}}{{\rm d}t} = \frac{\rm d}{{\rm d}t}\int \left(\frac{1}{2} m_{\rm i} v_\parallel^2 + \mu B\right) f\,{\rm d}^6 Z, \qquad (23)$$

$$\begin{aligned}\frac{{\rm d}E_{\rm fld}}{{\rm d}t} &= \int e\langle\phi\rangle_\alpha \frac{\partial f}{\partial t}\,{\rm d}^6 Z \\ &= \frac{\rm d}{{\rm d}t}\frac{1}{8\pi}\int\left[\frac{\rho_{\rm ti}^2}{\lambda_{\rm Di}^2}|\nabla_\perp\phi|^2 + \frac{1}{\lambda_{\rm De}^2}|\phi - \langle\phi\rangle_{\rm f}|^2\right]{\rm d}\boldsymbol{x}, \end{aligned}\qquad (24)$$

$$\frac{{\rm d}E_{\rm col}}{{\rm d}t} = \int e\langle\phi\rangle_\alpha C(f)\,{\rm d}^6 Z, \qquad (25)$$

$$\frac{{\rm d}E_{\rm src}}{{\rm d}t} = \int H S_{\rm src}\,{\rm d}^6 Z \sim P_{\rm in}, \qquad (26)$$

$$\begin{aligned}\frac{{\rm d}E_{\rm snk}}{{\rm d}t} &= \int H S_{\rm snk}\,{\rm d}^6 Z - \int [m_{\rm i}^2 B_\parallel^* \dot{\boldsymbol{R}} H f]_{\boldsymbol{R}=\boldsymbol{R}_{\rm b.c.}}\,{\rm d}v_\parallel\,{\rm d}\mu\,{\rm d}\alpha \\ &\quad - \int [m_{\rm i}^2 B_\parallel^* \dot{v}_\parallel H f]_{v_\parallel = v_{\parallel{\rm b.c.}}}\,{\rm d}\boldsymbol{R}\,{\rm d}\mu\,{\rm d}\alpha. \end{aligned}\qquad (27)$$

In the simulation, we impose the Dirichlet boundary condition $f = f_0$ at the boundary of a computational domain, $\boldsymbol{R} = \boldsymbol{R}_{\rm b.c.}$, $v_\parallel = v_{\parallel{\rm b.c.}}$, which leads to finite outgoing and incoming fluxes across the computational boundary. These boundary fluxes are taken into account in equation (27). It is noted that the boundary flux in a configuration space is absorbed by the sink term in a buffer region in the outside of the core plasma boundary, and f at the velocity space boundary is very small. Therefore, these boundary fluxes do not affect core plasmas so much. Equation (25) shows collisional power transfer due to the FLR effect, which is $\mathcal{O}(k_\perp^2\rho_{\rm ti}^2)$ contribution to the power balance. Although this power transfer is a spurious effect coming from a mismatch between the gyrokinetics and a drift-kinetic like collision operator, its influence on the power balance is negligible in the simulation (see figure 8).

In GT5D [1], the gyrokinetic Poisson bracket operator in equation (3) is discretized using the fourth order NDCFD, which enables robust and accurate computation of nonlinear turbulent dynamics based on a full-f approach. The gyrokinetic Poisson equation (9) is computed using toroidal mode expansion and a 2D finite element approximation on the poloidal plane. The linear Fokker–Planck operator (10) is discretized using the sixth order centred finite difference. It is noted that, in the simulation, conservation properties, equations (11)–(13), are not satisfied exactly because of small numerical errors coming from a finite difference operator and a truncated velocity space. In order to compensate these numerical errors in the collision operator, we add a correction term to the field particle operator. More details concerning an implementation of the collision operator are given in the appendix. The time integration is performed using the second order additive semi-implicit Runge–Kutta method [32] and a stiff linear term involving the parallel streaming is treated implicitly. The code consists of three components, a gyrokinetic solver in the cylindrical coordinates, $(R, \zeta, Z, v_\parallel, \mu)$, a Poisson solver in the flux coordinates, (r, θ, φ) and a Fokker–Planck solver in the moving frame, (u, s), where θ is the poloidal angle and $\varphi = -\zeta$ is the toroidal angle. In a configuration space, the cylindrical coordinates used in the gyrokinetic solver is less effective in resolving flute perturbations or ballooning modes aligned with the magnetic field. However, this approach enables straightforward treatments of the magnetic axis and open field regions in diverted tokamak configurations keeping conservation properties of the NDCFD [1]. Although this approach requires a transformation between (R, ζ, Z) and (r, θ, φ), a cost of the field solver including the transformation is ~5% in the simulations presented in section 4. In a velocity space, $(v_\parallel, \mu)$ or (u, s) coordinates are aligned to fine scale structures produced by ballistic modes, and the μ coordinate is useful for parallelization. However, the coordinates are less effective to capture trapped-passing boundaries. The accuracy of collisionless turbulent dynamics of GT5D was verified through linear and nonlinear ITG benchmark tests against GT3D, which is based on a mesh free Lagrangian approach, and reasonable agreements were confirmed [1]. On the other hand, the collision operator will be tested in neoclassical benchmark calculations in section 3. In long time source driven ITG turbulence simulations, the accuracy of the nonlinear simulation is monitored by checking the power balance (22).

3. Benchmark test of neoclassical transport

In the neoclassical benchmark, we solve the gyrokinetic equations (3) and (4) in the axisymmetric and sourceless limit to estimate the ion neoclassical transport in relevant kinetic equilibria. Although GT5D can simulate steep profiles and low aspect ratio configurations with finite orbit width effects, in the present benchmark, we use a circular concentric tokamak configuration with a relatively large aspect ratio ($R_0/a = 5, a/\rho_{\rm ti} \sim 150$, $q(r) = 0.85 + 2.18(r/a)^2$) and moderate density and temperature gradients ($R_0/L_n = 1$, $R_0/L_{\rm ti} = 1$) to make quantitative comparisons with standard local theories, where R_0 is the major radius, a is the minor radius, $L_n = |n_0(\mathrm{d}n_0/\mathrm{d}r)^{-1}|$ and $L_{\rm ti} = |T_{\rm i}(\mathrm{d}T_{\rm i}/\mathrm{d}r)^{-1}|$. In these parameters, the ratio of the ion banana orbit width Δ_b to $L_{\rm ti}$ is $\Delta_{\rm b}/L_{\rm ti} \sim 0.006$, where a local approach is a good approximation. The normalized collisionality is chosen as $\nu^* = 0.01$–10, and the parallel flow is given as $U_\parallel = -0.1v_{\rm ti}, 0, 0.1v_{\rm ti}$ corresponding to counter-, balance- and co-rotating tokamaks. From convergence tests, the time step width and the grid numbers are determined as $\Delta t = 4\Omega_{\rm i}^{-1}$ and $(N_R, N_\zeta, N_Z, N_{v\parallel}, N_\mu) = (160, 1, 160, 80, 20)$. We perform axisymmetric simulations starting from a local Maxwellian distribution $f_{\rm LM}$. Since $f_{\rm LM}$ does not annihilate the gyrokinetic Poisson bracket operator, the radial electric field $E_{\rm r}$ quickly develops in a transit time and the geodesic acoustic mode (GAM) is excited. Through the damping of GAMs, $E_{\rm r}$ develops to satisfy the ambipolar condition, and then, the system gradually approaches the neoclassical solution. Figure 1 shows the time histories of the particle flux Γ and the heat flux $Q_{\rm NC}$. As is noted in section 2, the physical model of the neoclassical simulation reduces to that of the neoclassical theory except for minor corrections such as remaining FLR effects on macroscopic perturbations. Therefore, in the present benchmark, we compare particle and heat fluxes defined following standard definitions in the neoclassical theory [27, 28]:

$$\Gamma \equiv \left\langle \int f(\boldsymbol{v}_B \cdot \nabla r) m_{\rm i}^2 B_\parallel^* \,\mathrm{d}v_\parallel \,\mathrm{d}\mu \,\mathrm{d}\alpha \right\rangle_{\rm f}, \tag{28}$$

$$Q_{\rm NC} \equiv \left\langle \int \left(\tfrac{1}{2} m_{\rm i} v_\parallel^2 + \mu B\right) f(\boldsymbol{v}_B \cdot \nabla r) m_{\rm i}^2 B_\parallel^* \,\mathrm{d}v_\parallel \,\mathrm{d}\mu \,\mathrm{d}\alpha \right\rangle_{\rm f} - \tfrac{5}{2} T_{\rm i} \Gamma. \tag{29}$$

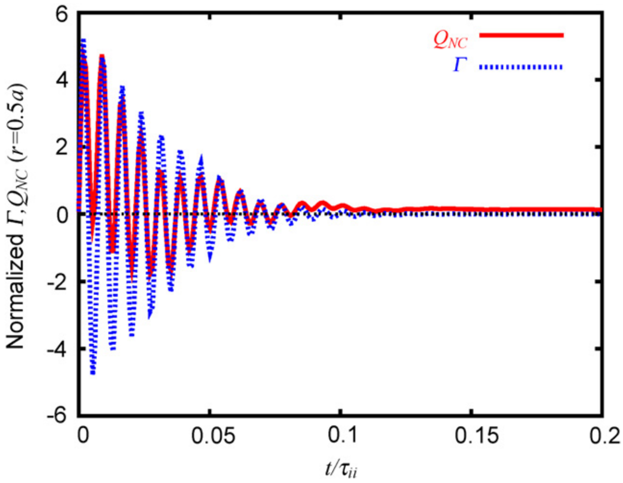

Figure 1. The particle flux Γ and the heat flux $Q_{\rm NC}$ observed at $r = 0.5a$ in a neoclassical benchmark simulation with $R_0/a = 5$, $\nu^* \sim 0.1$ and $U_\parallel \sim 0$. After transient damping of GAMs, Γ and $Q_{\rm NC}$ approach the ambipolar condition $\Gamma = 0$ and the neoclassical heat transport level, respectively.

Figure 1 shows transient evolutions of Γ and $Q_{\rm NC}$, respectively. Equation (16) leads to the ambipolar condition $\Gamma = 0$ in a steady state. In figure 1, this ambipolar condition is satisfied after the initial transient damping of GAMs. This result shows that the system follows the $E_{\rm r}$ equation (16). Then, the system enters a relaxation phase, where the heat flux coincides with the energy flux (the first term in the r.h.s. of equation (29)). It is noted that during GAM oscillations, $Q_{\rm NC}$ is positive on average. This heat flux is an order of magnitude larger than the neoclassical level, and is observed also in the collisionless limit. Since the present neoclassical simulation keeps only $(m, n) = (0, 0)$ component of the electric field, this flux is not produced by the $E \times B$ drift but by a coupling between up–down asymmetric GAM perturbations and the magnetic drift. This collisionless transport mechanism may be important when GAMs are excited in a plasma. Figure 2 shows $Q_{\rm NC}$ observed in simulations with $\nu^* \sim 0.1$ and $\nu^* \sim 1$, which give transport levels comparable to Chang–Hinton's formula (C–H formula) [33]. In figure 3, the neoclassical heat diffusivity $\chi_{\rm i} = -Q_{\rm NC}/(n_{\rm i}\nabla T_{\rm i})$ observed in GT5D agrees with that estimated from the C–H formula over a wide ν^* regime. Another important property of the ion neoclassical transport is the force balance relation among the parallel flow, the Pfirsh–Schlüter flow and the neoclassical poloidal flow. A force balance relation in the local neoclassical theory [27] is given as

$$\langle U_\parallel \rangle_{\rm f} = \frac{T_{\rm i} I}{m_{\rm i}\Omega_i}\left(\frac{\mathrm{d}\psi}{\mathrm{d}r}\right)\left[(k-1)\frac{\mathrm{d}\ln T_{\rm i}}{\mathrm{d}r} - \frac{\mathrm{d}\ln n_{\rm i}}{\mathrm{d}r} + \frac{e}{T_{\rm i}}E_{\rm r}\right], \tag{30}$$

where ψ is the poloidal flux, $I = RB_\zeta$, $n_{\rm i}$ is the ion density and $k = k(\nu^*)$ is a coefficient of the neoclassical poloidal flow. In figure 4, $E_{\rm r}$ in a steady state is plotted for counter-, balance- and co-rotating tokamaks, and the results show good agreement with those estimated from equation (30). In figure 5, $k(\nu^*)$ observed in GT5D is compared with equation (6.136) in [27] (H–H formula) and with a banana limit solution with a finite aspect ratio correction, $1.17F_{\rm c}$ (see equation (11.58) in [28]). It is noted that the former solution is obtained in the large aspect ratio limit $\epsilon = r/R_0 \to 0$, while the latter

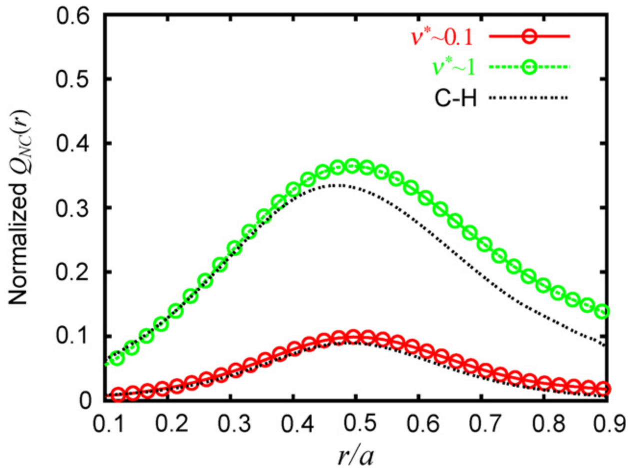

Figure 2. The radial profiles of the heat flux Q_{NC} observed at $t/\tau_{\mathrm{ii}} \sim 0.8$ in neoclassical benchmark simulations with $R_0/a = 5$, $\nu^* \sim 0.1$, 1 and $U_\parallel \sim 0$. Dotted lines show the heat flux estimated by Chang–Hinton's formula.

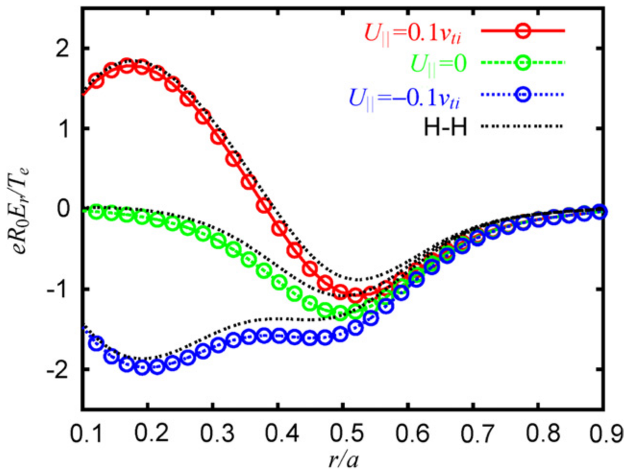

Figure 4. The radial electric field E_{r} observed at $t/\tau_{\mathrm{ii}} \sim 0.8$ in neoclassical benchmark simulations with $R_0/a = 5$, $\nu^* \sim 0.1$ and $U_\parallel \sim -0.1v_{\mathrm{ti}}, 0, 0.1v_{\mathrm{ti}}$. Dotted lines show E_{r} estimated using the force balance relation (30).

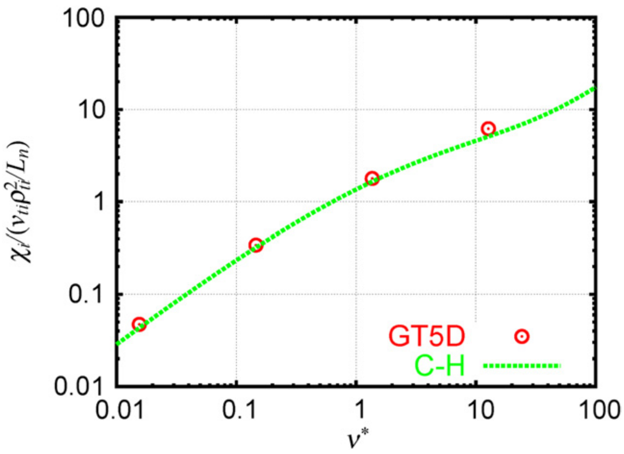

Figure 3. ν^* dependence of the neoclassical ion heat diffusivity χ_{i} observed at $r/a = 0.5$ in neoclassical benchmark simulations with $R_0/a = 5$, $\nu^* = 0.01$–10 and $U_\parallel \sim 0$. A dashed curve shows χ_{i} estimated by Chang–Hinton's formula.

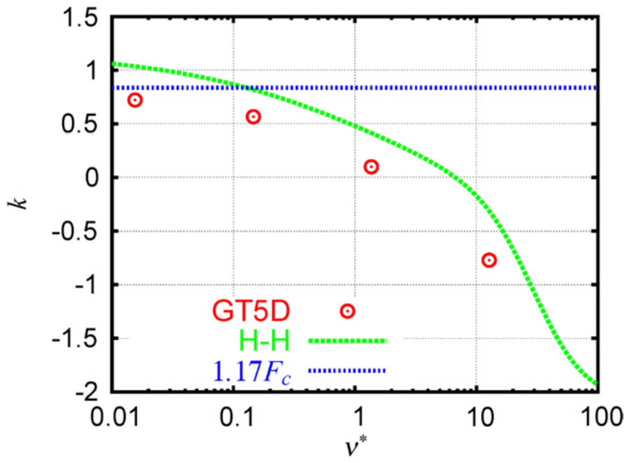

Figure 5. ν^* dependence of k observed at $r/a = 0.5$ in neoclassical benchmark simulations with $R_0/a = 5$, $\nu^* = 0.01$–10 and $U_\parallel \sim 0$. A dashed curve shows k estimated by equation (6.136) in [27]. A dotted line shows a banana limit solution multiplied by the finite ratio correction F_{c} [28].

solution takes account of a finite aspect ratio effect through a factor $F_{\mathrm{c}} = f_{\mathrm{p}}/(f_{\mathrm{p}} + 0.462 f_{\mathrm{t}})$, where the effective fraction of trapped particles is $f_{\mathrm{t}} \sim 1.46\sqrt{\epsilon}$ and $f_{\mathrm{p}} = 1 - f_{\mathrm{t}}$. Over a wide ν^* regime, $k(\nu^*)$ shows qualitatively similar behaviour as the H–H formula, and a flip of the poloidal rotation in the collisional regime is captured. However, in the banana regime, k is close to $1.17F_{\mathrm{c}}$ rather than the H–H formula. A similar discrepancy in k between neoclassical simulations and the H–H formula in the banana regime was reported also in [34]. These benchmark results show that GT5D can determine E_{r} self-consistently by evolving equilibrium profiles. It is noted that in the neoclassical simulation, χ_{i} and k reach steady state values at $t \sim \tau_{\mathrm{ii}}$. This gives a minimum time duration required to have the neoclassical physics in gyrokinetic simulations, where τ_{ii} is the ion–ion collision time.

In the present neoclassical benchmarks, standard local neoclassical theories are recovered in the steady state, and the collision operator is verified quantitatively. In addition, the present axisymmetric simulations clarified transient behaviour of collisional and collisionless transport processes, which cannot be explained in the framework of conventional neoclassical theory.

4. Source driven ITG turbulence simulation

In the present study, we use a circular concentric tokamak configuration with $R_0/a = 2.79$, $a/\rho_{\mathrm{ti}} = \rho^{*-1} \sim 150$, 1/3 wedge torus and $q(r) = 0.85 + 2.18(r/a)^2$, which gives cyclone like parameters [35], $r_{\mathrm{s}}/R_0 \sim 0.18$, $q(r_{\mathrm{s}}) \sim 1.4$ and $\hat{s}(r_{\mathrm{s}}) = [(r/q)\,\mathrm{d}q/\mathrm{d}r]_{r=r_{\mathrm{s}}} \sim 0.78$ at $r_{\mathrm{s}} = 0.5a$. In this configuration, simulation parameters are chosen as follows: the time step width is $\Delta t = 2\Omega_{\mathrm{i}}^{-1}$, grid numbers used in the gyrokinetic solver and the Fokker–Planck solver are $(N_R, N_\zeta, N_Z, N_{v\parallel}, N_\mu) = (160, 32, 160, 80, 20)$, finite elements used in the field solver are $(N_r, N_\theta) = (150, 150)$ and the system size is $R - R_0 = -1.07a$–$1.07a$ ($\Delta R = 2\rho_{\mathrm{ti}}$), $Z = -1.07a$–$1.07a$ ($\Delta Z = 2\rho_{\mathrm{ti}}$), $\zeta = 0 \sim 2\pi/3$ ($n = 0, 3, 6, \ldots, 48$), $v_\parallel = -5v_{\mathrm{ti}} \sim 5v_{\mathrm{ti}}$, $\sqrt{2\mu B_0/m_{\mathrm{i}}} = 0$–$5v_{\mathrm{ti}}$, where n is the toroidal mode number

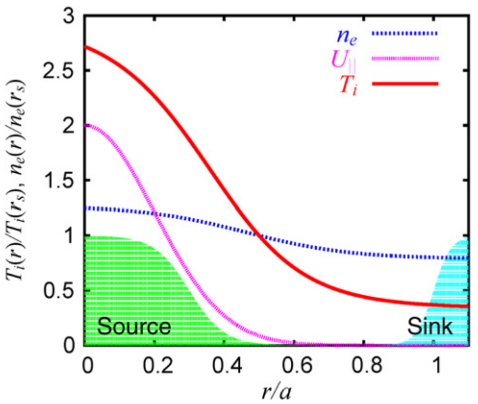

Figure 6. The initial n_e, $U_\parallel$, T_i profiles and deposition profiles of A_{src} and A_{snk}.

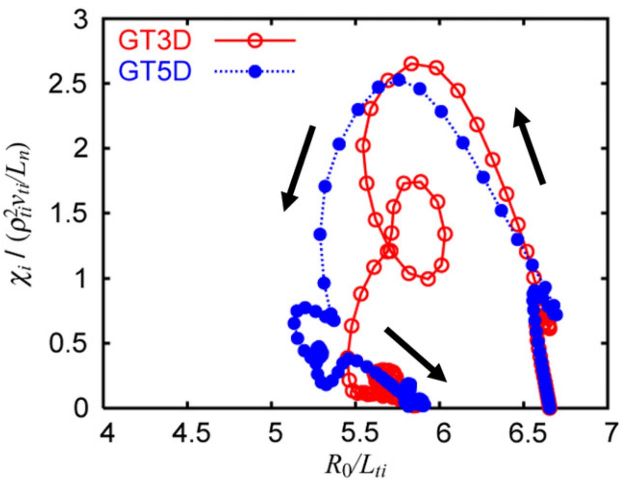

Figure 7. The time evolutions of χ_i and R_0/L_{ti} observed at $r/a = 0.5 \pm 0.0625$ in collisionless and sourceless ITG benchmark simulations with cyclone like parameters [1]. Arrows show time histories. After the transient saturation of ITG modes, profile relaxation occurs towards nonlinear marginal states. Results from GT5D and GT3D converge to the same nonlinear critical gradient $R_0/L_{ti} \sim 6$, where the ion heat transport is quenched.

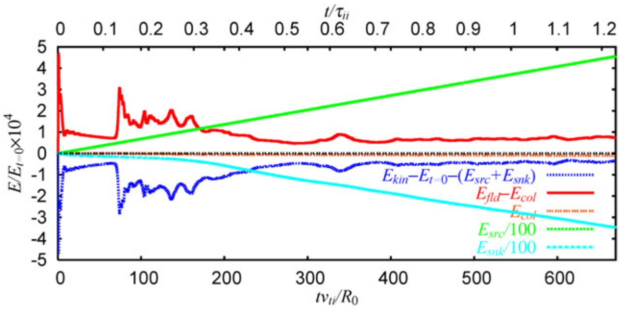

Figure 8. The time histories of the kinetic energy E_{kin}, the field energy E_{fld}, the collisional power transfer E_{col}, the input power E_{src} and the output power in the sink E_{snk} in the source driven ITG turbulence simulation with $P_{in} = 2$ MW. The plot is normalized by the initial kinetic energy $E_{t=0}$, and E_{src} and E_{snk} are scaled by 1/100. In the plot, the energy conservation is shown by a balance between $E_{fld} - E_{col}$ and $E_{kin} - E_{t=0} - (E_{src} + E_{snk})$. After $tv_{ti}/R_0 \sim 300$, a power balance condition, $\dot{E}_{src} + \dot{E}_{snk} \sim 0$, is established.

and B_0 is the magnetic field at the magnetic axis. Here, $n = 48$ corresponds to $k_\theta \rho_{ti} \sim 1$ at $r/a = 0.5$ and $k_\theta \rho_{ti} \sim 0.65$ at $r/a = 0.9$, respectively. The velocity space resolution is determined by neoclassical benchmark calculations, which suggest lower velocity space resolution than previous collisionless ITG turbulence simulations [1], because of the collisional dissipation of fine scale velocity space structures. Figure 6 shows the initial n_e, $U_\parallel$ and T_i profiles, and the deposition profiles of A_{src} and A_{snk}. In the initial condition, a weak co-rotation is given to study momentum transport, and the ion temperature profile is far above linear and nonlinear thresholds at $R_0/L_{ti} \sim 4.5$ and $R_0/L_{ti} \sim 6$, respectively. Here, this nonlinear threshold value is identified using two different gyrokinetic codes, GT5D and GT3D, through collisionless and sourceless ITG benchmark simulations with similar cyclone like parameters [1] (see figure 7). Plasma parameters at $r = r_s$ are $n_e = n_i \sim 5 \times 10^{19}\,\mathrm{m}^{-3}$, $T_e \sim T_i \sim 2$ keV, $R_0/L_n = 2.22$, $R_0/L_{te} = 6.92$, $R_0/L_{ti} = 10.0$ and $\nu^* \sim 0.025$. Near the magnetic axis, the heat source model (7) is given by f_{M1} ($n_i = \bar{n}_i$, $U_\parallel = 0$, $T_i = 2\bar{T}_i$) and f_{M2} ($n_i = \bar{n}_i$, $U_\parallel = 0$, $T_i = \bar{T}_i$), where $\bar{n}_i$ and $\bar{T}_i$ are the volume averaged density and temperature. Power scan simulations with $P_{in} = 2$ MW and $P_{in} = 4$ MW are performed, where τ_{src} is determined by equation (21) and the source deposition profile A_{src} is chosen to be broad enough so that the heating process does not produce negative values of f in the heating region. It is noted that P_{in} is defined as power input in a full torus configuration, and therefore, practical power input is $P_{in}/3$ in a 1/3 wedge torus configuration. In a boundary region, the time constant in the sink model (8) is given as $\tau_{snk}^{-1} = 0.1 v_{ti}/a$. This parameter is chosen to be large enough to fix $U_\parallel$ and T_i in the boundary region. Since the present simulation model satisfies a power balance in a steady state and the heat flux is imposed by input power P_{in}, the simulation is not so sensitive to τ_{snk}, provided that the sink is strong enough and the boundary conditions for $U_\parallel$ and T_i are unchanged.

Figure 8 shows the time histories of the kinetic energy E_{kin}, the field energy E_{fld}, the collisional power transfer E_{col}, the input power E_{src} and the output power in the sink E_{snk} in the simulation with $P_{in} = 2$ MW. In the simulation, we trace long time evolutions of the ITG turbulence and equilibrium profiles over $\sim 1.2\tau_{ii}$ or $\sim 10^3 \tau_c$, where τ_c is the correlation time of the turbulent fields. The simulation is initialized using f_{LM} as in the previous neoclassical benchmark, leading to the initial excitation of E_r and GAMs. After the damping of GAMs, the system relaxes towards a kinetic equilibrium condition, $\{f, H\} \sim C(f)$. However, in the simulation with non-axisymmetric components, the ITG mode shows linear growth, provided that R_0/L_{ti} exceeds the nonlinear threshold. In the initial nonlinear phase, the saturation of linear ITG modes shows transient bursts, which produce an order of magnitude larger heat transport than the quasi-steady transport level. Although these initial bursts due to linear ITG modes are unphysical phenomena, their large heat transport quickly adjusts the T_i profile towards nonlinear marginal states in turbulent time scales. In collisionless and sourceless ITG turbulence simulations, the turbulent transport is almost quenched after these bursts [1] (see figure 7). However, in the present source driven ITG simulation, the turbulent transport is sustained by constant power input, and a power balance condition, $\dot{E}_{src} + \dot{E}_{snk} \sim 0$, is established in physically meaningful quasi-steady states. In figure 8, the energy conservation (9), which is shown by a balance between

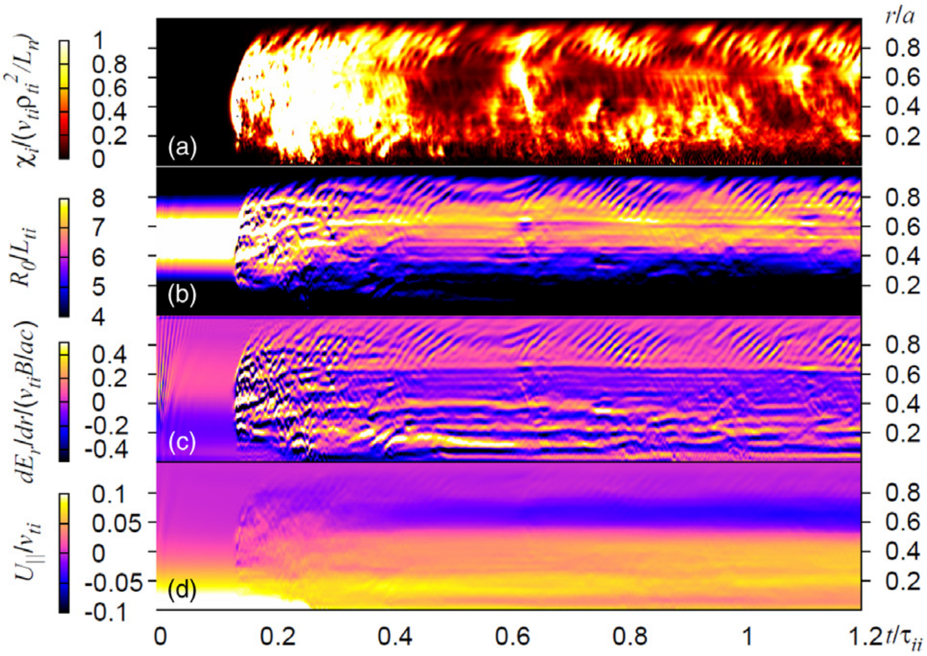

Figure 9. The spatio-temporal evolutions of (*a*) the ion heat diffusivity χ_i, (*b*) the normalized ion temperature gradient R_0/L_{ti}, (*c*) the radial electric field shear dE_r/dr and (*d*) the parallel flow $U_\parallel$ in a simulation with $P_{in} = 2$ MW.

$E_{fld} - E_{col}$ and $E_{kin} - E_{t=0} - (E_{src} + E_{snk})$, is satisfied for a long time in the quasi-steady state. This is the stringent verification of long time source driven ITG turbulence simulations.

Figure 9 shows the spatio-temporal evolutions of the ion heat diffusivity χ_i, the normalized ion temperature gradient R_0/L_{ti}, the radial electric field shear dE_r/dr, and the parallel flow $U_\parallel$. Here, the ion heat diffusivity $\chi_i = -Q/(n_i\nabla T_i)$ is defined using the turbulent heat flux

$$Q \equiv \left\langle \int \left(\tfrac{1}{2}m_i v_\parallel^2 + \mu B\right) f(\dot{\boldsymbol{R}}_1\cdot\nabla r) m_i^2 B_\parallel^* \, dv_\parallel \, d\mu \, d\alpha \right\rangle_f , \quad (31)$$

where $\dot{\boldsymbol{R}}_1 = \{\boldsymbol{R}, \tilde{H}\}$ is given by a non-axisymmetric part of the Hamiltonian, $\tilde{H} = H - \langle H\rangle_\zeta$, and n_i and T_i are given by evolving equilibrium profiles. Although the time history of E_{fld} suggests a quasi-steady turbulent state, figure 9 indicates active turbulent dynamics. Remarkable features found in the source driven ITG turbulence simulation are that the turbulent transport in a source free region ($r/a = 0.5$–0.9) is dominated by active avalanches (see figure 9(*a*)), and the T_i profile in this region is tied to globally constant L_{ti} at $R_0/L_{ti} \sim 6.5$, which is slightly above the nonlinear critical value at $R_0/L_{ti} \sim 6$ (see figures 9(*b*) and 10(*b*)). It is noted that in figure 10(*b*), R_0/L_{ti} at $r/a = 0.5$ is very close to the cyclone parameter $R_0/L_{ti} = 6.92$. While the radial correlation length $\Delta r_c \sim 5\rho_{ti}$ and the correlation time $\tau_c \sim 0.7R_0/v_{ti} \sim 2a/v_{ti}$ of the turbulent fields suggest a gyro-Bohm like picture, the propagation width and the fastest time scale of avalanches observed in the simulation with $P_{in} = 2$ MW show an order of magnitude larger scales $l_A \sim 20\rho_{ti}$ and $\tau_A \sim 9R_0/v_{ti}$, respectively. Their propagation velocity estimated from space–time autocorrelation analyses shows a ballistic feature with $V_A \sim \rho_{ti}v_{ti}/R_0$. It is noted that in this simulation, GAM activities are not observed except for the initial relaxation phase, and the time scale of avalanches $\omega_A \sim 2\pi/\tau_A \sim 0.7v_{ti}/R_0$ is slower than that of GAMs $\omega_{GAM} \sim 2v_{ti}/R_0$. The avalanche propagation of heat flux with similar spatio-temporal scales was reported also in other gyrokinetic simulations [7, 36]. In the power scan, it is found that with increasing P_{in} from 2 to 4 MW, Q is doubled with almost the same L_{ti}, showing strong profile stiffness (see figure 10). Here, there is no significant change in Δr_c and τ_c, and the increase of χ_i is mainly due to enhanced amplitudes of avalanches. In figure 11, it is shown that a significant part of the turbulent heat transport is produced by avalanches, and their amplitudes are almost doubled with increasing P_{in} from 2 to 4 MW. These avalanches propagate with almost the same velocity, but the propagation width becomes shorter $l_A \sim 10\rho_{ti}$ because of stronger T_i corrugation and local E_r shear, which suppresses the ballistic propagation of avalanches. Although τ_A is not changed so much, a quasi-periodic feature becomes weak in the autocorrelation function of Q, and an intermittent feature becomes strong. In figure 12, the power spectrum of Q shows a small peak at ω_A, where the power law changes from $1/\omega$ to stronger decay. This kind of $1/f$ type spectrum is a typical feature of SOC like phenomena [12].

In figure 9, not only χ_i but also L_{ti} and dE_r/dr show similar avalanches. According to cross correlation analyses, both L_{ti} and E_r show a delay $\Delta t \sim 1.5R_0/v_{ti}$ from χ_i, but there is no delay between L_{ti} and E_r. This suggests that avalanche components of E_r are determined by some local force balance or equilibrium condition. It is noted that the radial electric field E_r in the present source driven ITG turbulence simulations is qualitatively different from that observed in the collisionless and sourceless ITG turbulence simulations, which are dominated by quasi-steady zonal flows [1]. In figure 13, it is found that quasi-steady zonal flows are observed only in a core region ($r/a < 0.4$), and a source free region ($r/a > 0.4$) is dominated by mean E_r and avalanches. Although turbulence driven zonal flows have been considered as an important saturation mechanism in the ITG turbulence, the source free region, which is close to nonlinear marginal states, is not subject to this picture, and

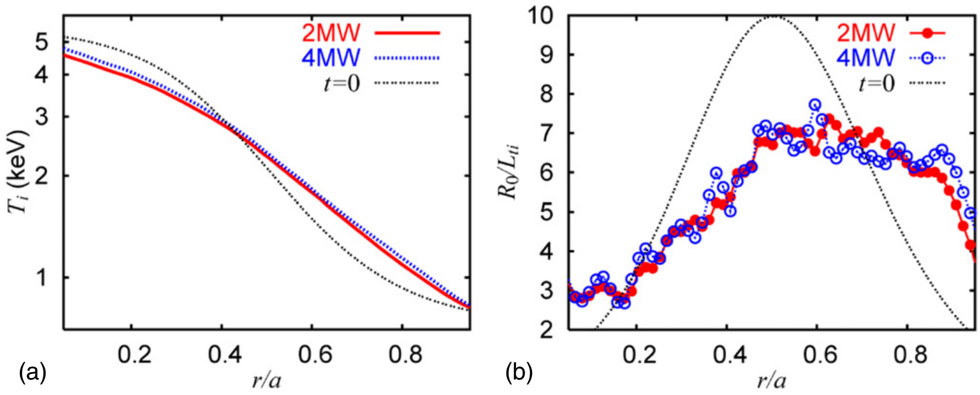

Figure 10. The quasi-steady profiles (time average over $tv_{\rm ti}/R_0 = 400$–650) of (*a*) $T_{\rm i}$ (log scale) and (*b*) $L_{\rm ti}$ observed in power scan simulations with $P_{\rm in} = 2$ MW and $P_{\rm in} = 4$ MW. Similar quasi-steady profiles are observed in two simulations with different input power, showing strong profile stiffness. Both profiles are far from the initial condition (dotted curve), and source free regions ($r/a = 0.5$–0.9) are tied to globally constant $L_{\rm ti}$ ($R_0/L_{\rm ti} \sim 6.5$) near the nonlinear critical value ($R_0/L_{\rm ti} \sim 6$).

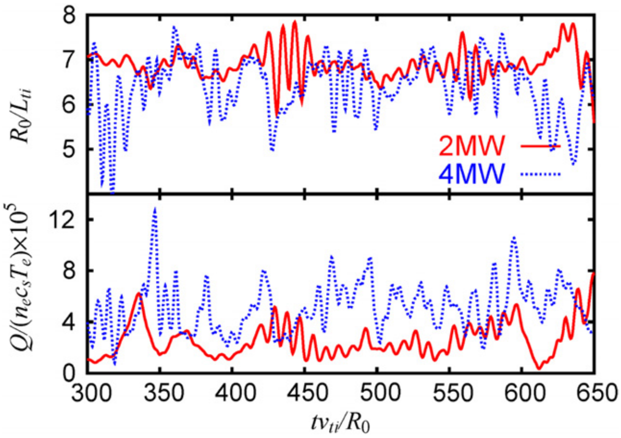

Figure 11. The time histories of $L_{\rm ti}$ and Q at $r/a = 0.7$. The time average of $\chi_{\rm i}/(v_{\rm ti}\rho_{\rm ti}^2/L_n)$ over $tv_{\rm ti}/R_0 = 400$–650 is ~0.4 and ~0.8 for $P_{\rm in} = 2$ MW and $P_{\rm in} = 4$ MW, respectively. The neoclassical heat transport is less than $\chi_{\rm i}/(v_{\rm ti}\rho_{\rm ti}^2/L_n) \sim 0.1$.

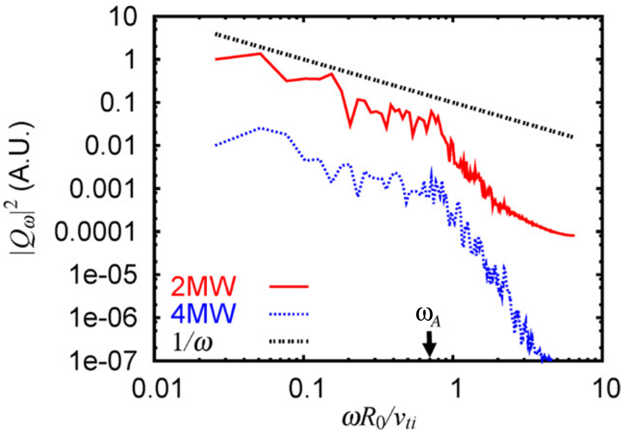

Figure 12. The power spectrum of the turbulent heat flux Q averaged over source free regions ($r/a = 0.5$–0.9). The spectra in low frequency region show $1/f$ type spectra.

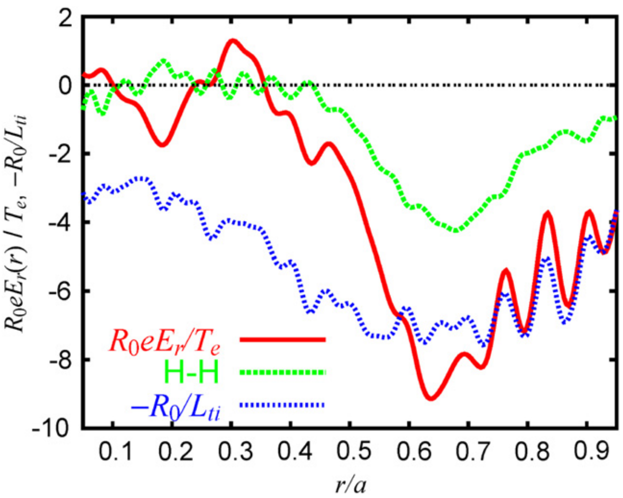

Figure 13. The radial profiles of $E_{\rm r}$ and $L_{\rm ti}$ observed in a simulation with $P_{\rm in} = 2$ MW ($tv_{\rm ti}/R_0 \sim 550$). 'H–H' shows $E_{\rm r}$ estimated by a force balance relation (30) with the H–H formula.

other effects such as mean $E_{\rm r}$ flows and avalanche phenomena dictate turbulent transport levels. As a mechanism of Bohm scaling, the importance of mean flows near marginal states was pointed out in [9, 37]. In the source free region, mean $E_{\rm r}$ is significantly larger than that estimated from the force balance relation (30) with the H–H formula. In order to understand this discrepancy, we compare a radial profile of k against the H–H formula, $1.17F_{\rm c}$, and a neoclassical GT5D simulation in the axisymmetric limit, $k_{\rm GT5D}$. It is noted that from the viewpoint of the ratio $\Delta_{\rm b}/L_{\rm ti} \sim 0.08$, the local neoclassical theory seems to be still valid. In figure 14, k is smaller than the H–H theory, but is close to $k_{\rm GT5D}$, which shows a similar radial dependence as $1.17F_{\rm c}$. Therefore, a discrepancy between k and the H–H formula can be explained by taking account of a finite aspect ratio effect coming from $F_{\rm c}$, and k is not so far from the neoclassical level. To understand the remaining discrepancy between k and $k_{\rm GT5D}$, further investigations on effects of turbulent fluctuations and fluctuating equilibrium profiles on the neoclassical physics are needed. Because of relatively small k, $E_{\rm r}$ in the source free region is determined mainly by a force balance between the parallel flow and the Pfirsh–Schlüter flow. As a result, avalanche components of $E_{\rm r}$ show a clear correlation with $R_0/L_{\rm ti}$ in figure 13.

The shear of equilibrium $E_{\rm r}$ affects propagation of avalanches. In figure 9, the propagation direction of avalanches is changed depending on the sign of $dE_{\rm r}/dr$. At $r/a < 0.6$ ($r/a > 0.6$), the $E_{\rm r}$ shear is negative (positive) on average,

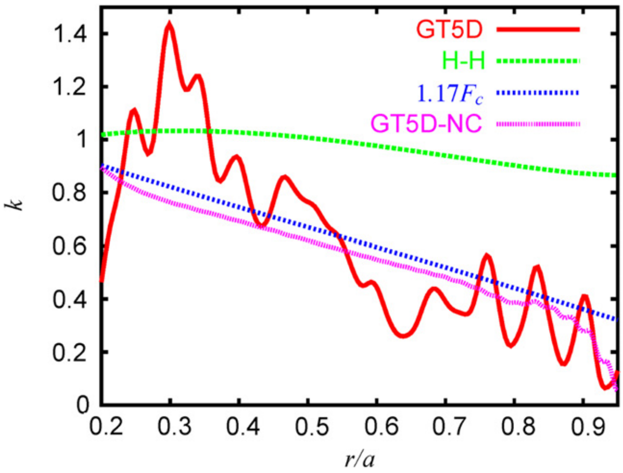

Figure 14. The radial profiles of k (solid) estimated for E_r in figure 13. Also plotted are the H–H formula, $1.17F_c$ and k obtained from an axisymmetric simulation of GT5D.

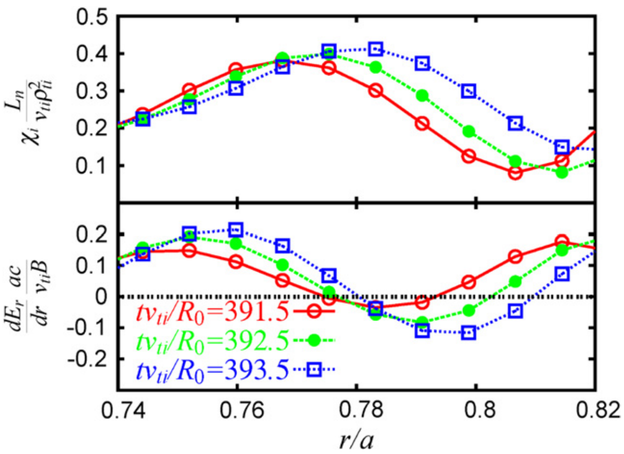

Figure 15. Radial propagation of avalanche fronts observed in a simulation with $P_{in} = 2$ MW. The avalanche fronts, where χ_i shows local peaks, are bounded by positive and negative E_r shear shifted by mean E_r shear.

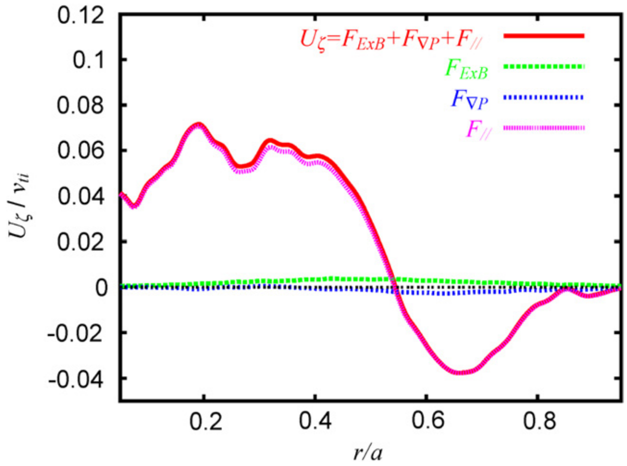

Figure 16. The toroidal rotation profile observed at $t = \tau_{ii}$ in a simulation with $P_{in} = 2$ MW. Co-rotation is sustained in a core region ($r/a = 0$–0.5) without momentum input. On the other hand, a notch structure of counter-rotation is formed in a source free region ($r/a = 0.5$–0.9). $F_\parallel$, $F_{E\times B}$, and $F_{\nabla P}$, respectively, show toroidal projection of parallel flows, perpendicular $E \times B$ flows and perpendicular diamagnetic flows.

and avalanches propagate inwards (outwards). This can be understood from a relation between E_r and L_{ti}. In the avalanche front, flattening of T_i occurs, and local maxima of E_r and $-R_0/L_{ti}$ are produced following a local force balance relation (see figure 13). As a result, the avalanche front is bounded by positive and negative local E_r shear regions where local E_r shear is shifted on average by mean E_r shear (see figure 15). In the positive (negative) mean E_r shear region, local E_r shear outside (inside) is always weaker than the other side, and ITG modes in the avalanche front tend to couple with modes outside (inside), leading to one-sided propagation of avalanches. This mechanism may explain a change in the direction of the avalanche propagation depending on toroidal rotation reported in [7].

Another important effect of the E_r shear is its influence on the momentum transport. Before discussing the momentum transport, we discuss a difference between the parallel flow and the toroidal rotation. Figure 16 shows the toroidal rotation profile and its parallel, perpendicular $E \times B$ and perpendicular ∇P components observed at $t = \tau_{ii}$. Although the parallel and perpendicular flows observed are the same order in the simulation with zero momentum input, toroidal projection of the latter becomes an order of magnitude smaller than the former. Therefore, we focus only on the parallel momentum and its transport. In the present simulation, initial parallel flows with $U_\parallel/v_{ti} \sim 0.1$ are given in the co-current direction, and the momentum diffusion is observed during initial transient bursts leading to a relaxation of the $U_\parallel$ profile (see figures 9(*d*) and 17(*a*)). However, in the quasi-steady turbulent state, co-rotation in the core region and counter-rotation in the source free region build up without momentum input, which suggests the existence of non-diffusive momentum transport. In order to see the uniqueness of this rotation profile, we perform the same simulation starting from $U_\parallel \sim 0$. In the simulation, properties of turbulent ion heat transport and T_i profiles are not changed. Figure 17(*b*) shows evolutions of the $U_\parallel$ profile observed in the simulation. Here, small initial parallel flows with $U_\parallel \sim 0.02v_{ti}$ come from the $v_\parallel$ dependence of the Jacobian $m^2B_\parallel^*$. The result shows that even with different initial conditions, similar co-rotation in the core region and counter-rotation in the source free region build up without momentum input. This means that the rotation profiles are intrinsic. It should be noted that in figure 9, the heat transport and the T_i profile are in the quasi-steady state after transient bursts. However, $U_\parallel$ is slowly evolving even in this stage, while its evolution rate becomes slower in the later phase. Since this level of $U_\parallel$ does not work as a turbulence drive, the $U_\parallel$ profile is not stiff and its evolution is slow.

The turbulent momentum transport consists of the momentum diffusion, the momentum pinch [38, 39] and the E_r shear stress [40, 41]. Since the rotation profile builds up even from the initial condition with $U_\parallel \sim 0$, the E_r shear stress is considered to play a role in the momentum pinch observed. In figure 18, the time averaged momentum flux Π is in the opposite direction to the momentum gradient or $-\mathrm{d}U_\parallel/\mathrm{d}r$, showing a non-diffusive feature. Here, the turbulent parallel momentum flux Π is defined as

$$\Pi \equiv \left\langle \int v_\parallel f(\dot{\boldsymbol{R}}_1 \cdot \nabla r) m_i^2 B_\parallel^* \,\mathrm{d}v_\parallel \,\mathrm{d}\mu \,\mathrm{d}\alpha \right\rangle_f . \qquad (32)$$

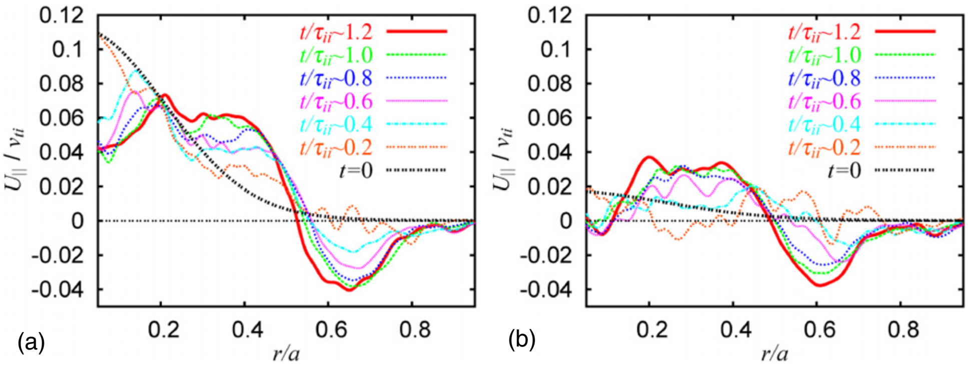

Figure 17. The time evolutions of parallel flow profiles observed in simulations starting from (*a*) $U_\parallel \sim 0.1v_{\rm ti}$ and (*b*) $U_\parallel \sim 0$. Other simulation parameters are the same. Simulations starting from different initial $U_\parallel$ profiles approach similar rotation profiles without momentum input.

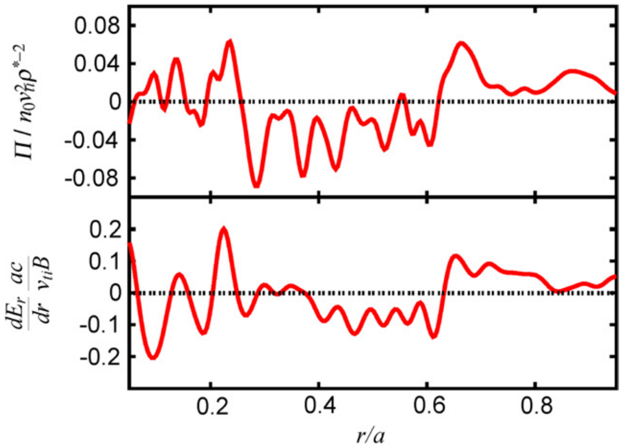

Figure 18. The momentum flux Π and the radial electric field shear $\mathrm{d}E_{\rm r}/\mathrm{d}r$ observed in a simulation with $P_{\rm in} = 2\,\mathrm{MW}$ (time average over $tv_{\rm ti}/R_0 = 400$–650).

Figure 18 also shows a correlation between Π and $\mathrm{d}E_{\rm r}/\mathrm{d}r$, and Π is outwards (inwards) in a positive (negative) $\mathrm{d}E_{\rm r}/\mathrm{d}r$ region at $r/a > 0.6$ ($r/a = 0.4$–0.6). Although this result shows a signature of the E_r shear stress, a quantitative balance among the above three mechanisms is complicated especially after the rotation profile builds up. In [42], the relative importance of these mechanisms was quantitatively investigated by δf flux-tube simulations, where $U_\parallel$, $\mathrm{d}U_\parallel/\mathrm{d}r$ and $\mathrm{d}E_{\rm r}/\mathrm{d}r$ are imposed. In contrast, in the present full-f global simulations, all these parameters are self-consistently determined through complicated nonlinear processes. On the one hand, $U_\parallel$ is determined by the turbulent momentum transport, and $U_\parallel$ and evolving equilibrium profiles dictate $E_{\rm r}$ through a force balance relation. On the other hand, the non-diffusive momentum transport depends on $U_\parallel$ and $\mathrm{d}E_{\rm r}/\mathrm{d}r$, and turbulence suppression due to $\mathrm{d}E_{\rm r}/\mathrm{d}r$ also affects the turbulent momentum transport. Although full-f simulations are useful to dictate the intrinsic toroidal rotation through the above complicated nonlinear processes, further investigations are needed to understand each mechanism separately.

5. Summary

In this work, long time source driven ITG turbulence simulations are developed by extending sources and collisions in a global gyrokinetic toroidal full-f 5D Vlasov code GT5D. The key features of GT5D are summarized as follows.

1. The NDCFD enables robust and accurate long time full-f simulations, where the turbulent transport and equilibrium profiles are evolved self-consistently based on the same first principles.
2. Ion–ion collisions are implemented using the linear Fokker–Planck collision operator, which is important not only as a physically relevant dissipation mechanism of fine scale velocity space structures but also as the neoclassical physics which dictates the equilibrium $E_{\rm r}$ and a baseline of transport levels.
3. Choices (and extensions) of source and sink models are flexible. In this work, two source models are developed reflecting conditions of on-axis heating and H-mode like edge plasmas.

The collision operator is verified through benchmark calculations of the neoclassical transport, in which standard local neoclassical theories are recovered in the quasi-steady phase. However, in the transient phase, it is found that significant heat transport is driven by GAMs, and that the heat diffusivity and the poloidal rotation approach the neoclassical levels slowly in a collision time, which gives the minimum time duration to simulate the neoclassical physics.

Source driven ITG turbulence simulations in a normal shear tokamak with $\rho^{*-1} \sim 150$ and $\nu^* = 0.025$–0.1 are performed using the source models to fix power input (zero momentum input) near the axis and $T_{\rm i}$ and $U_\parallel$ ($\sim$0) at the edge. In the simulation, long time behaviour of the turbulent transport and profile formations is traced over a collision time, and the following key features of the ion turbulent transport are clarified:

1. The $T_{\rm i}$ profile in a source free region is tied to globally constant $L_{\rm ti}$ near the nonlinear threshold, and strong stiffness is observed in the power scan. This kind of stiff $T_{\rm i}$ profile with globally constant $L_{\rm ti}$ was typically observed in H-mode plasmas in JT60U [43].
2. In the source free region, a significant part of the heat flux is carried by avalanche like phenomena, which have an order of magnitude larger spatio-temporal scales than the radial correlation length $\Delta r_{\rm c} \sim 5\rho_{\rm ti}$ and the correlation time $\tau_{\rm c} \sim 2a/v_{\rm ti}$ of the turbulent fields. This suggests a possibility of non-local or Bohm like features of the turbulent transport produced by gyro-Bohm like turbulent fields.

3. The intermittent heat flux of avalanches shows $1/f$ type spectra, which are typically observed in SOC like phenomena. Similar $1/f$ type spectra were observed also in the experiment [44]. The criticality of $L_{\rm ti}$ and $1/f$ type spectra suggests that stiff $T_{\rm i}$ profiles produced in the ITG turbulence may be explained by a SOC type picture.
4. Roles of the mean $E_{\rm r}$ shear are found. The $E_{\rm r}$ shear dictates the direction of the avalanche propagation. The mean $E_{\rm r}$ shear profile and the non-diffusive momentum flux show a clear correlation. This suggests a signature of the $E_{\rm r}$ shear stress.
5. Without momentum input near the axis, non-diffusive momentum transport keeps non-zero toroidal rotation in the co- (counter-) current direction in the core (outer) region, which may be related to the intrinsic toroidal rotation in the experiment [45, 46].

These features show, at least, qualitative agreement with the experiment, and suggest the validity of the source driven ITG turbulence simulation using GT5D. Since GT5D has a capability of using shaped MHD equilibria and equilibrium profiles in the JT60U database, further quantitative validation will be addressed.

The SOC like phenomena of the ion heat transport is a unique feature observed in the full-f gyrokinetic simulation, and may be related to non-local or Bohm like features of the turbulent transport. To study their impact on the turbulent transport in future large devices, we need ρ^* scan with full-f gyrokinetic simulations. In this study, non-diffusive momentum fluxes are observed and their correspondence with the $E_{\rm r}$ shear stress is discussed. However, a detailed balance among the momentum diffusion, the momentum pinch and the $E_{\rm r}$ shear stress as well as the Prantl number have not been identified, yet. To study the momentum transport further in detail, we need simulations with different momentum input. These simulations will be addressed in future works.

Acknowledgments

One of the authors (YI) would like to thank Drs H. Sugama, S. Satake, T.-H. Watanabe, M. Honda, N. Hayashi and M. Kikuchi for useful comments on the neoclassical calculation. He is also grateful to Drs P.H. Diamond, M. Yoshida and Y. Kamada for stimulating discussions on non-diffusive momentum transport. The simulations were performed on the JAEA Altix3700Bx2 system. This work is supported by the MEXT, Grant No 18760647.

Appendix A. Implementation of collision operator

By neglecting FLR corrections, the linear Fokker–Planck collision operator [25] is given as

$$C(f) = C_T(f) + C_{\rm F}, \tag{A1}$$

$$C_T(f) = \frac{\partial}{\partial s}(\nu_{\perp 1}v^2 f) + \frac{\partial}{\partial u}(\nu_{\parallel 1}uf) + \frac{1}{2}\frac{\partial^2}{\partial s^2}(\nu_{\perp 2}v^4 f) + \frac{1}{2}\frac{\partial^2}{\partial u^2}(\nu_{\parallel 2}v^2 f) + \frac{\partial^2}{\partial s \partial u}(\nu_{\parallel\perp}v^3 f), \tag{A2}$$

$$C_{\rm F} = P f_{\rm M}, \tag{A3}$$

where $s = 2\mu B/m_{\rm i}$ and $u = v_\parallel - U_\parallel$ consist of a moving frame with respect to the parallel flow velocity $U_\parallel$, $v^2 = u^2 + s$ and $f_{\rm M}$ is a shifted Maxwellian distribution defined by the density, the parallel flow and the temperature at each local position. By using relations

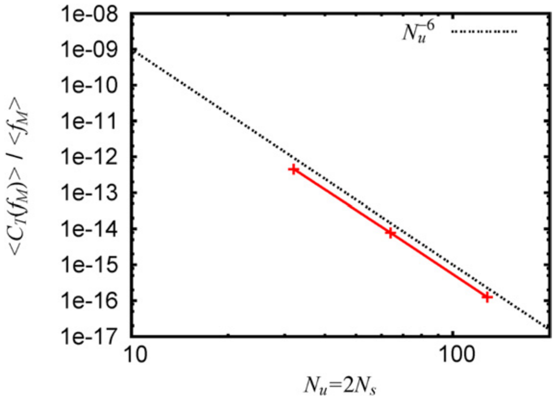

Figure 19. The convergence test of the test particle operator. The remaining errors of $\int C_T(f_{\rm M})\,{\rm d}^3v/\int f_{\rm M}\,{\rm d}^3v$ are plotted against the velocity grid number $N_{v\parallel} = 2N_{v\perp}$.

$$\hat{F} = 2\nu_0\Psi(x), \tag{A4}$$

$$\hat{G} = \frac{1}{2}\nu_0 v^2\left[\left(1 - \frac{1}{2x}\right)\Psi(x) + \Psi'(x)\right], \tag{A5}$$

$$\hat{H} = -\frac{1}{2}\nu_0 v^2\left[\left(1 - \frac{3}{2x}\right)\Psi(x) + \Psi'(x)\right], \tag{A6}$$

collision frequencies in the test particle operator are written as

$$\nu_{\perp 1} = \frac{2s}{v^2}\hat{F} - \frac{4}{v^2}\hat{G} - \frac{2s}{v^4}\hat{H}, \tag{A7}$$

$$\nu_{\parallel 1} = \hat{F}, \tag{A8}$$

$$\nu_{\perp 2} = \frac{2}{v^4}\left(4s\hat{G} + \frac{4s^2}{v^2}\hat{H}\right), \tag{A9}$$

$$\nu_{\parallel 2} = \frac{2}{v^2}\left(\hat{G} + \frac{u^2}{v^2}\hat{H}\right), \tag{A10}$$

$$\nu_{\parallel\perp} = \frac{4su}{v^5}\hat{H}, \tag{A11}$$

where $\Psi(x) = {\rm erf}(\eta) - \eta\,{\rm erf}'(\eta)$ is the Maxwellian integral, ${\rm erf}(\eta)$ is the error function, $x = \eta^2$, $\eta = v/(\sqrt{2}v_{\rm t})$, $v_{\rm t} = \sqrt{T_{\rm i}/m_{\rm i}}$ is a local thermal velocity, $\nu_0 = (4\pi n_{\rm e}e^4)/(m_{\rm i}^2 v^3)\ln\Lambda$ and $\ln\Lambda$ is the Coulomb logarithm. We further rewrite the test particle operator as

$$C_T(f) = C(1)f + \nu_{\rm s}v^2\frac{\partial f}{\partial s} + \frac{1}{2}\nu_{\perp 2}v^4\frac{\partial^2 f}{\partial s^2} + \frac{1}{2}\nu_{\parallel 2}v^2\frac{\partial^2 f}{\partial u^2} + \nu_{\parallel\perp}v^3\frac{\partial^2 f}{\partial s\partial u}, \tag{A12}$$

$$C(1) = \nu_0\sqrt{\frac{2}{\pi}}\left(\frac{v}{v_t}\right)^3 {\rm e}^{-x}, \tag{A13}$$

$$\nu_{\rm s} = \nu_{\perp 1} + \frac{\partial}{\partial s}(\nu_{\perp 2}v^2) + \frac{\partial}{\partial u}(\nu_{\parallel\perp}v). \tag{A14}$$

In equation (A12), all the coefficients are calculated analytically by substituting equilibrium parameters estimated at each local position, and derivatives of f are obtained by the sixth order centred finite difference scheme. In order to see the accuracy of the test particle collision operator, its annihilation property with respect to $f_{\rm M}$ is tested and the remaining errors are plotted against the velocity grid number $N_{v\parallel} = 2N_{v\perp}$. In figure 19, the remaining errors are proportional to $N_{v\parallel}^{-6}$.

Table 1. The conservation properties of the collision operator observed for $C(f_C)$ with $N_{v\parallel} = 2N_{v\perp} = 32$–128 and $v_{\parallel\max} = v_{\perp\max} = 5v_t$. The conservation of momentum and energy is satisfied with C_F. All the conservation properties are further improved up to the machine precision compared with C_T by adding C_{corr}.

	C_T	$C_T + C_F$	$C_T + C_F + C_{corr}$
$\frac{1}{n_0}\int C\,d^3v(N_{v\parallel} = 32)$	−0.2541E–11	−0.1997E–11	−0.2104E–23
$\frac{1}{m_i n_0 v_{ti}}\int m_i v_\parallel C\,d^3v(N_{v\parallel} = 32)$	0.1868E−09	−0.3587E–11	−0.1654E–24
$\frac{2}{3n_0T_i}\int \frac{1}{2}m_i v^2 C\,d^3v(N_{v\parallel} = 32)$	0.1226E−09	−0.2722E–11	−0.1613E–23
$\frac{1}{n_0}\int C\,d^3v(N_{v\parallel} = 64)$	−0.5189E–12	−0.6802E–12	−0.9947E–23
$\frac{1}{m_i n_0 v_{ti}}\int m_i v_\parallel C\,d^3v(N_{v\parallel} = 64)$	0.1801E−09	−0.1162E–11	0.1780E−24
$\frac{2}{3n_0T_i}\int \frac{1}{2}m_i v^2 C\,d^3v(N_{v\parallel} = 64)$	0.1282E−09	−0.2120E–11	−0.5898E–23
$\frac{1}{n_0}\int C\,d^3v(N_{v\parallel} = 128)$	0.1739E−12	−0.1711E–12	−0.2381E–23
$\frac{1}{m_i n_0 v_{ti}}\int m_i v_\parallel C\,d^3v(N_{v\parallel} = 128)$	0.1782E−09	−0.5210E–12	−0.1326E–24
$\frac{2}{3n_0T_i}\int \frac{1}{2}m_i v^2 C\,d^3v(N_{v\parallel} = 128)$	0.1290E−09	−0.1967E–11	−0.1702E–22

In the field particle operator (A3), a function P, which is determined from the momentum and energy conservation, is written as [26]

$$P = -3\sqrt{\frac{\pi}{2}}\Psi\eta^{-3}u\hat{p} - 3\sqrt{\frac{\pi}{2}}\left[\Psi - \Psi'\right]\eta^{-1}\hat{E}, \tag{A15}$$

$$\hat{p} = \frac{1}{nv_t^2}\int uC_T(f)\,d^3v, \tag{A16}$$

$$\hat{E} = \frac{1}{3nv_t^2}\int u^2C_T(f)\,d^3v. \tag{A17}$$

With this field particle operator, $C(f)$ conserves the particle number, the momentum and the energy. However, the conservation property is not exactly satisfied with a finite velocity grid number and a limited velocity space. Although the remaining numerical error is small compared with f, its accumulation (in particular, erroneous particle accumulation) in a long time simulation may not be negligible compared with δf. In order to compensate the remaining error, we add a correction term given by

$$C(f) = C_T(f) + C_F + C_{corr}, \tag{A18}$$

$$C_{corr} = \nu_{corr}(f_{M1} - f_{M2}), \tag{A19}$$

where ν_{corr} is a constant and f_{M1} and f_{M2} are determined in an iterative manner to satisfy the conservation properties, equations (11)–(13). Table 1 shows the conservation properties observed when the collision operator is operated on a test function given by a gyrokinetic Vlasov equilibrium $f_C(P_\zeta, \varepsilon, \mu)$ defined at $r/a = 0.5$ and $\theta = 0$ in a cyclone like configuration used in section 4. The results show that the errors of momentum and energy are cancelled by C_F. However, by adding C_{corr}, all the conservation properties are improved up to the machine precision compared with the original errors in C_T.

References

[1] Idomura Y. *et al* 2008 Conservative global gyrokinetic toroidal full-f five-dimensional Vlasov simulation *Comput. Phys. Commun.* **179** 391

[2] Villard L. *et al* 2004 First principle based simulations of instabilities and turbulence *Plasma Phys. Control. Fusion* **46** B51

[3] Tang W.M. and Chan V.S. 2005 Advances and challenges in computational plasma science *Plasma Phys. Control. Fusion* **47** R1

[4] Waltz R.E. *et al* 2005 Advances in comprehensive gyrokinetic simulations of transport in tokamaks *Nucl. Fusion* **45** 741

[5] Idomura Y., Watanabe T.-H. and Sugama H. 2006 Kinetic simulations of turbulent fusion plasmas *C. R. Phys.* **7** 650

[6] Doyle E.J. *et al* 2007 Progress in the ITER Physics Basis Chapter 2: Plasma confinement and transport *Nucl. Fusion* **47** S18

[7] Candy J. and Waltz R.E. 2003 Anomalous transport scaling in the DIII-D tokamak matched by supercomputer simulation *Phys. Rev. Lett.* **91** 045001

[8] Holland C. *et al* 2008 Validation of gyrokinetic transport simulations using DIII-D core turbulence measurements *Proc. 22nd Int. Conf. on Fusion Energy 2008 (Geneva, Switzerland, 2008)* (Vienna: IAEA) CD-ROM file TH/8-1 and http://www-naweb.iaea.org/napc/physics/FEC/FEC2008/html/index.htm

[9] Waltz R.E., Candy J. and Rosenbluth M.N. 2002 Gyrokinetic turbulence simulation of profile shear stabilization and broken gyroBohm scaling *Phys. Plasmas* **9** 1938

[10] Carreras B.A. *et al* 1996 A model realization of self-organized criticality for plasma confinement *Phys. Plasmas* **3** 2903

[11] Garbet X. and Waltz R.E. 1998 Heat flux driven ion turbulence *Phys. Plasmas* **5** 2836

[12] Bak P., Tang C. and Wiesenfeld K. 1987 Self-organized criticality: an explanation of $1/f$ noise *Phys. Rev. Lett.* **59** 381

[13] Diamond P.H. and Hahm T.S. 1995 On the dynamics of turbulent transport near marginal stability *Phys. Plasmas* **2** 3640

[14] Grandgirard V. *et al* 2007 Global full-f gyrokinetic simulations of plasma turbulence *Plasma Phys. Control. Fusion* **49** B173

[15] Xu X.Q. *et al* 2007 Edge gyrokinetic theory and continuum simulations *Nucl. Fusion* **47** 809

[16] Haikkinen J.A. *et al* 2008 Full f gyrokinetic method for particle simulation of tokamak transport *J. Comput. Phys.* **227** 5582

[17] Chang C.S. *et al* 2009 Compressed ITG turbulence in diverted tokamak edge *Phys. Plasmas* **16** 056108

[18] Idomura Y. *et al* 2007 New conservative gyrokinetic full-f Vlasov code and its comparison to gyrokinetic δf particle-in-cell code *J. Comput. Phys.* **226** 244

[19] Idomura Y., Tokuda S. and Kishimoto Y. 2003 Global gyrokinetic simulation of ion temperature gradient driven turbulence in plasmas using a canonical Maxwellian distribution *Nucl. Fusion* **43** 234

[20] Lee W.W. and Tang W.M. 1988 Gyrokinetic particle simulation of ion temperature gradient drift instabilities *Phys. Fluids* **31** 612

[21] Krommes J.A. and Hu G. 1994 The role of dissipation in the theory and simulations of homogeneous plasma turbulence, and resolution of the entropy paradox *Phys. Plasmas* **1** 3211

[22] Sugama H. *et al* 1966 Transport processes and entropy production in toroidal plasmas with gyrokinetic electromagnetic turbulence *Phys. Plasmas* **3** 2379

[23] Watanabe T.-H. and Sugama H. 2004 Kinetic simulation of steady states of ion temperature gradient driven turbulence with weak collisionality *Phys. Plasmas* **11** 1476

[24] Brizard A.J. and Hahm T.S. 2007 Foundations of nonlinear gyrokinetic theory *Rev. Mod. Phys.* **79** 421

[25] Xu X.Q. and Rosenbluth M.N. 1991 Numerical simulation of ion-temperature-gradient-driven modes *Phys. Fluids* B **3** 627

[26] Wang W.X. *et al* 1999 A new δf method for neoclassical transport studies *Plasma Phys. Control. Fusion* **41** 1091

[27] Hinton F.L. and Hazeltine R.D. 1976 Theory of plasma transport in toroidal confinement systems *Rev. Mod. Phys.* **48** 239

[28] Helander P. and Sigmar D.J. 2002 *Collisional Transport in Magnetized Plasmas* (Cambridge: Cambridge University Press)

[29] Wang W.X., Hinton F.L. and Wong S.K. 2001 Neoclassical radial electric field and transport with finite orbits *Phys. Rev. Lett.* **87** 055002

[30] Satake S. *et al* 2005 Non-local neoclassical transport simulation of geodesic acoustic mode *Nucl. Fusion* **45** 1362

[31] Parra F.I. and Catto P.J. 2008 Limitations of gyrokinetics on transport time scales *Plasma Phys. Control. Fusion* **50** 065014

[32] Zhong X. 1996 Additive semi-implicit Runge–Kutta methods for computing high-speed nonequilibrium reactive flows *J. Comput. Phys.* **128** 19

[33] Chang C.S. and Hinton F.L. 1982 Effect of finite aspect ratio on the neoclassical ion thermal conductivity in the banana regime *Phys. Fluids* **25** 1493

[34] Belli E.A. and Candy J. 2008 Kinetic calculation of neoclassical transport including self-consistent electron and impurity dynamics *Plasma Phys. Control Fusion* **50** 095010

[35] Dimits A.M. *et al* 2000 Comparisons and physics basis of tokamak transport models and turbulence simulations *Phys. Plasmas* **7** 969

[36] McMillan B.F, *et al* 2008 Long global gyrokinetic simulations: source terms and particle noise control *Phys. Plasmas* **15** 052308

[37] Garbet X. and Waltz R.E. 1996 Action at distance and Bohm scaling of turbulence in tokamaks *Phys. Plasmas* **3** 1898

[38] Peeters A.G., Angioni C. and Strintzi D. 2007 Toroidal momentum pinch velocity due to the coriolis drift effect on small scale instabilities in a toroidal plasma *Phys. Rev. Lett.* **98** 265003

[39] Hahm T.S. *et al* 2008 Turbulent equipartition theory of toroidal momentum pinch *Phys. Plasmas* **15** 055902

[40] Dominguez R.R. and Steabler G.M. 1993 Anomalous momentum transport from drift wave turbulence *Phys. Fluids* B **5** 3876

[41] Gürcan Ö.D. *et al* 2007 Intrinsic rotation and electric field shear *Phys. Plasmas* **14** 042306

[42] Waltz R.E. *et al* 2007 Gyrokinetic theory and simulation of angular momentum transport *Phys. Plasmas* **14** 122507

[43] Urano H. *et al* 2008 Dependence of heat transport on toroidal rotation in conventional H-modes in JT-60U *Nucl. Fusion* **48** 085007

[44] Politzer P.A. 2000 Observation of avalanchelike phenomena in a magnetically confined plasma *Phys. Rev. Lett.* **84** 1192

[45] Rice J.E. *et al* 2007 Inter-machine comparison of intrinsic toroidal rotation in tokamaks *Nucl. Fusion* **47** 1618

[46] Yoshida M. *etal* 2008 Role of pressure gradient on intrinsic toroidal rotation in tokamak plasmas *Phys. Rev. Lett.* **100** 105002